



HAL
open science

The influence of incoming turbulence on the dynamic modes of an NREL-5MW wind turbine wake

Giovanni de Cillis, Stefania Cherubini, Onofrio Semeraro, Stefano Leonardi,
Pietro de Palma

► **To cite this version:**

Giovanni de Cillis, Stefania Cherubini, Onofrio Semeraro, Stefano Leonardi, Pietro de Palma. The influence of incoming turbulence on the dynamic modes of an NREL-5MW wind turbine wake. *Renewable Energy*, 2022, 183, pp.601 - 616. 10.1016/j.renene.2021.11.037 . hal-03498440

HAL Id: hal-03498440

<https://hal.science/hal-03498440>

Submitted on 6 Jan 2022

HAL is a multi-disciplinary open access archive for the deposit and dissemination of scientific research documents, whether they are published or not. The documents may come from teaching and research institutions in France or abroad, or from public or private research centers.

L'archive ouverte pluridisciplinaire **HAL**, est destinée au dépôt et à la diffusion de documents scientifiques de niveau recherche, publiés ou non, émanant des établissements d'enseignement et de recherche français ou étrangers, des laboratoires publics ou privés.

The influence of incoming turbulence on the dynamic modes of an NREL-5MW wind turbine wake

Giovanni De Cillis¹, Stefania Cherubini^{1,*}, Onofrio Semeraro³, Stefano Leonardi², Pietro De Palma¹

Abstract

Knowledge of the dynamics of wind turbine wakes and its dependence on the incoming boundary layer is fundamental to optimize and control the power production of wind farms. This work aims at investigating the effect of inflow turbulence on the wake of the NREL-5MW wind turbine. Sparsity-Promoting Dynamic Mode Decomposition (SP-DMD) is performed on snapshots extracted from large-eddy simulations of the turbine wake, for detecting the most dynamically-relevant flow structures in the presence or absence of inflow turbulence. We demonstrate that inflow turbulence generated by a precursor simulation radically changes the most dynamically-relevant flow structures. For the laminar-inflow case the DMD modes selected by the SP algorithm have high wavenumbers and are spatially localized. When turbulence is added at the inflow, these high-frequency modes are superseded by low-frequency modes lying in the frequency range of the wake meandering and filling the whole domain, mostly corresponding to those dynamically relevant for the precursor simulation. These results show that, in the presence of inflow turbulence, coherent structures linked to endogenous mechanisms such as tip and root vortices lose their dynamical relevance in favour of those exogenously excited by turbulence, indicating that low-dimensional models of turbine wakes should take into account atmospheric turbulence.

Keywords: NREL 5MW wind turbine, DMD modes, uniform or turbulent inflow, turbulent precursor simulation

1. Introduction

Wind energy represents one of the fundamental renewable energy sources to meet the imminent climate goals provided for 2050, with an expected electricity production of about 35% of the total demand [1]. To reach this goal, an increase of the actual wind energy production is needed, which can be achieved by increasing the number of installed wind turbines and/or the size of the rotor disks and, at the same time, by improving the efficiency of new turbines and wind farms. Such an acceleration in the deployment of wind power installations requires the enhancement of policy support initiatives, eradication of regulatory uncertainties, and further investments in new technologies [2]. Concerning the wind turbine innovation, the trend towards increasing rotor diameters and hub heights is leading to a single-unit power production of 5–6 MW in the case of onshore applications (from an average of 2.6 MW in 2018), using diameters of 160–170 m. In the case of offshore installations, a single wind turbine will achieve 15–20 MW in the next 10–20 years, with diameters of about 230 m and hub heights of 150 m. Moreover, the optimization of the farm design, concerning, for instance, the turbine layout, and

*stefania.cherubini@poliba.it

¹DMMM, Politecnico di Bari, Via Re David 200, 70125, Bari, Italy

²Dept. of Mech. Eng., University of Texas, Dallas, Texas, USA

³LISN, Université de Paris-Saclay, CNRS, Orsay, France

38 its control become crucial to guarantee high efficiency, flexibility and security of the power
39 generation.

40 When clustered into farms, wind turbines are aerodynamically coupled to each-other in a
41 very complex way through the action of their wakes [3, 4]. A turbine in the wake of another may
42 produce up to 40% less energy depending on the distance between them and on the turbulence
43 intensity of the wind. The interaction becomes stronger when one attempts to increase the
44 power density of the plant by reducing the distance among the turbines. Several innovative
45 approaches can be exploited to optimize the farm efficiency and power density by controlling
46 the axial induction [5, 6] or the wake direction [7, 6] of each turbine. In particular, strategies
47 based on adjusting the rotor yaw angle have recently been proposed [7]. This technique consists
48 of creating a yaw misalignment between the turbine rotor and the incoming wind, so that the
49 wake is deflected laterally. As a consequence of the yaw misalignment, the efficiency of the
50 upstream turbine decreases, but the power production of the downstream turbine increases due
51 to the lateral deflection of the incoming wake. Another technique consists of tilting the rotor
52 axis away from the mean wind direction in the vertical plane, so that the wake of the front
53 turbine is redirected towards the ground, increasing the mean wind available to downstream
54 turbines. A combined effect of optimal variation of yaw and tilt angles has been shown to
55 guarantee a power increase of about 15% for two-row wind-aligned array of turbines [6].

56 Moreover, one has to consider that the hub heights of innovative wind turbines are higher
57 than 100 m, so that the rotors are immersed in the atmospheric boundary layer (ABL) and the
58 incoming flow is characterized by a streamwise velocity gradient along the vertical direction.
59 Such a gradient influences the blade loading, increasing the load on the blades pointing upwards
60 in the ABL [8]. Therefore, any attempt of optimizing the performance of a wind farm, taking
61 into account the interactions among the turbines, should include the effect of the shear of the
62 ABL and its modifications. In fact, the wake produced by a wind turbine is characterized by dif-
63 ferent flow structures which can be originated by endogenous or exogenous mechanisms. The
64 flow structures triggered by endogenous mechanisms are those produced by an isolated turbine
65 subject to a laminar inlet velocity, such as the tip- and root-vortex helices or the von Kármán
66 street developing behind the tower, as well as other structures arising downstream. However,
67 the wake of a wind turbine could be significantly influenced by flow structures embedded in
68 the ABL. In fact, coherent structures are detected in wind turbine wakes, which are not directly
69 generated by the turbine but are triggered by exogenous phenomena. These coherent structures
70 are different from those due to endogenous mechanisms and from those embedded in the ABL,
71 since they are generated by the interaction between the ABL and the turbine. The nature of
72 the incoming flow has a relevant effect on the operational state of the turbine and on the dy-
73 namics of its wake, including the main features of the turbulence generated by the turbine and
74 the recovery of the wake. In particular, numerical [9] and experimental data [10, 11] indicate
75 that single-turbine wakes recover faster with higher turbulence intensity levels in the incoming
76 flows. Moreover, in the case of uniform inflow, the interaction between the incoming wind and
77 the turbine generates an axisymmetric shear layer with axisymmetric turbulence statistics [9].
78 Instead, the typical non-uniform ABL velocity profile (logarithmic for neutral conditions) and
79 its turbulence distribution induce a higher level of turbulent kinetic energy production in the
80 upper part of the wake, due to the shear [12]. However, the influence of atmospheric turbulence
81 on the development of coherent structures in the wake, originated by endogenous or exogenous
82 mechanisms, has not been investigated in detail.

83 The present work aims at filling this gap by assessing or by quantifying the effect of a

84 turbulent incoming flow on the coherent structures characterising the wake of the NREL-5MW
85 reference wind turbine using a Sparsity-Promoting Dynamic Mode Decomposition (SP-DMD)
86 for the detection of dynamically-relevant flow structures. The flow through the NREL-5MW
87 wind turbine has been chosen as a realistic reference test case for a MW-scale wind turbine,
88 since the details of the turbine's geometry and a complete set of flow data are extensively
89 documented in literature and used in previous studies [13]. The DMD method was proposed by
90 Schmid [14]. The mathematical meaning of DMD modes is discussed in Ref. [15], where the
91 DMD modes are interpreted as a data-driven approximation of the Koopman modes, based on
92 a sequence of flow-field snapshots. The DMD method consists of finding the eigenvalues and
93 the eigenvectors of a linear operator approximating the non-linear dynamics embedded in the
94 data sequence and it has been recently exploited for the formulation of reduced order models
95 (ROMs) of wind-turbine flows [16, 17, 18]. DMD is applied to time-resolved data, such as
96 a sequence of snapshots obtained from numerical or experimental analyses, to determine the
97 dominant mechanisms characterizing the dynamics of the flow, namely, the DMD modes. Such
98 modes are non-orthogonal and are characterized by a single time frequency, so that they can be
99 sorted by their spectral contribution and spatial growth rate. This can be particularly interesting
100 for the design of a wind farm layout, since one can analyse which modes conserve a relevant
101 energy contribution downstream of a wind turbine and which frequencies are involved in the
102 dynamic load acting on downstream turbines. The interested reader can find further details on
103 the numerous DMD variants in Ref. [19].

104 DMD has been recently applied to the flow over a wind turbine. In particular, Sarmast et al.
105 [20] employed the DMD approach to study numerically a single wind turbine wake, focusing on
106 the tip-vortex instability onset, using the actuator line method. In Ref.s [16, 17, 18], reduced-
107 order models of wind turbine wakes were developed, using the DMD method based on Large
108 Eddy Simultaion (LES) flow data and considering different operational regimes. Premaratne
109 & Hu [21] provided an experimental study of the flow behind a horizontal-axis wind turbine
110 subject to a typical atmospheric boundary layer wind under neutral stability conditions. A high-
111 resolution digital particle image velocimetry was employed to obtain the snapshot sequence,
112 which was analyzed by the DMD method. Le Clainche et al. [18] employed the DMD method
113 based on Lidar measurements to build a reduced-order model of the wind velocity upstream of
114 a horizontal-axis wind turbine. Kleine et al. [22] provided a numerical study of the tip vortex
115 instability in two in-line turbines using the actuator-line method and the DMD approach. Sun et
116 al. [23] recently employed an LES to compute the unsteady flow over a two-blade wind turbine
117 model. They analyzed the wake flow using the DMD method in the absolute and in the relative
118 (with respect to the rotor) reference frames.

119 In general, only a limited number of DMD modes are relevant for the interaction among
120 turbines, allowing one to simplify the interaction model for optimization purposes [16]. DMD
121 modes are usually ranked according to their amplitude corresponding to the first snapshot of
122 the data-sequence. Using such a criterion for sorting the modes and selecting a limited number
123 of most significant modes can fail in capturing the relevant dynamics of the phenomena under
124 consideration, leading to low-accurate predictive capability of the generated low-dimensional
125 models. For this reason, several variants of the standard DMD algorithm, aiming at extracting a
126 limited subset of relevant flow features that optimally approximate the original data sequence,
127 have been developed, such as the Sparsity-Promoting-DMD [24]. In the present work we use
128 such a version of the algorithm, for the first time in wind turbine wake characterization, for
129 ranking the most relevant DMD modes.

130 The aim of this study is to investigate the effect of incoming turbulence on the most rele-
 131 vant coherent structures embedded in the turbulent wake flow developing downstream of the
 132 NREL-5MW wind turbine, using the SP-DMD approach. The proposed analysis is particularly
 133 relevant to optimise the energy production capacity of wind farms, on which the dynamics of
 134 the turbine wakes has a critical effect. The snapshot data-base is obtained through LES, per-
 135 formed in the absence and in the presence of inlet turbulence. The actuator line method is used
 136 for simulating the rotor, whereas, tower and nacelle are modeled with the immersed bound-
 137 ary method [25, 26]. The wind-turbine flow is simulated firstly imposing a laminar uniform
 138 inlet velocity profile and then considering a turbulent incoming flow generated by a precursor
 139 simulation. The incoming turbulent wind profile and its statistics have been generated by a
 140 preliminary LES considering a staggered-cube-array roughness distribution at wall simulating
 141 the landscape canopies [27]. Sparsity-promoting DMD is performed on the turbine wake with
 142 both uniform and turbulent inlet conditions, and on the precursor simulation itself, for compar-
 143 ison. It is found that the presence of inlet turbulence strongly affects the spatial structure and
 144 temporal frequency of the selected DMD modes.

145 The paper is structured as follows. In Sect. 2, the LES and DMD framework is described.
 146 The flow settings for the precursor and turbine wake simulations are presented in Sect. 3. In
 147 Sect. 4, the results of DMD of the flow fields obtained by LES are presented and discussed.
 148 Finally, in Sect. 5, the main results are summarized and conclusions drawn.

149 2. Methodologies

150 2.1. Large Eddy Simulation

Large Eddy Simulation (LES) of the wake behind the NREL-5MW wind turbine is car-
 ried out by solving the following governing equations for the filtered non-dimensional velocity
 components, u_i , where $i \in \{1, 2, 3\}$ indicate the streamwise, x , wall-normal, y , and spanwise,
 z , directions and the pressure p :

$$\frac{\partial u_i}{\partial t} + \frac{\partial u_i u_j}{\partial x_j} = -\frac{\partial p}{\partial x_i} + \frac{1}{Re} \frac{\partial^2 u_i}{\partial x_j \partial x_j} - \frac{\partial \tau_{ij}}{\partial x_j} + F_i, \quad (1)$$

$$\frac{\partial u_i}{\partial x_i} = 0. \quad (2)$$

The Reynolds number is defined as $Re = \frac{U_\infty D}{\nu}$, where U_∞ is the inlet velocity at the hub height,
 D is the rotor diameter and ν is the kinematic viscosity of the fluid, which have been used as
 reference variables for non-dimensionalisation. Concerning the residual stress tensor, τ_{ij} , while
 its isotropic part is included in the modified filtered pressure as $p^* = p + \frac{1}{3}\tau_{ii}$, its anisotropic part
 has to be modelled. Here we use the Smagorinsky model, based on the linear eddy viscosity
 hypothesis that relates the residual stress to the filtered rate of strain, S_{ij} , according to the
 following equation,

$$\tau_{ij}^r = -2\nu_r S_{ij}, \quad (3)$$

where the proportionality constant ν_r is the eddy viscosity of residual motions. The latter is, in
 turn, modelled using the mixing length hypothesis as:

$$\nu_r = l_S^2 \mathcal{S} = (C_S \Delta)^2 \mathcal{S}, \quad (4)$$

151 where \mathcal{S} is the characteristic filtered rate of strain, defined as $\mathcal{S} \equiv (2S_{ij}S_{ij})$, and l_S is the
 152 Smagorinsky length-scale, which is defined as the product between the Smagorinsky constant
 153 C_S and the filter width Δ . The Smagorinsky constant is set to 0.17, whereas the filter width is
 154 defined as the cube root of the local cell volume.

The governing equations (1) are solved using a second-order-accurate centered finite difference scheme on a staggered Cartesian grid and a hybrid low-storage third-order-accurate Runge-Kutta scheme for time integration [28]. Note that the last term in equation (1), F_i , represents the force per unit volume given by the actuator line method [29], which models the forces exerted by the turbine blades on the fluid by means of the lift and drag coefficients C_L, C_D . Approximating the rotor blades as rotating rigid lines divided into discrete segments, each one associated with a relative inflow velocity, u_{rel} , and an angle of attack, α , one can estimate the lift and drag forces (per unit length) as:

$$F_L = \frac{1}{2}\rho u_{rel}^2 C_L(\alpha) c F, \quad (5)$$

$$F_D = \frac{1}{2}\rho u_{rel}^2 C_D(\alpha) c F, \quad (6)$$

155 where ρ is the fluid density, c is the chord, F is the modified Prandtl correction factor accounting
 156 for the aerodynamic effect of the tip and root vortices [25]. These forces are then spread on
 157 areas perpendicular to each actuator line using a Gaussian distribution kernel. The tower and
 158 nacelle are modeled by the immersed boundary method, using a discrete forcing approach
 159 [30, 31]. The overall method has been extensively validated in the case of wind turbines [25,
 160 26]. The code has also been coupled with WRF to simulate a real wind farm in north Texas.
 161 Numerical results agreed very well with SCADA data [32].

162 2.2. Sparsity Promoting Dynamic Mode Decomposition

The Dynamic Mode Decomposition (DMD) [15, 14], is a data-driven technique capable of extracting dynamically relevant flow structures by assuming a linear mapping between successive snapshots. The variant employed in the present study is called Sparsity Promoting Dynamic Mode Decomposition (SP-DMD) and was proposed by Jovanović et al. [24]. The main idea is to carry out a constrained error minimization for optimally reconstructing the data-set using selecting only a limited number of DMD modes. The first step is to collect, from numerical simulations or experimental findings, snapshots of the flow field, $\mathbf{q}^i \in \mathbb{C}^N$, at a constant sampling frequency. Each snapshot has dimension $N = O \times S$, O being the number of observables, S representing the number of measurements points. Let us consider M snapshots and assume a linear time-invariant mapping \mathbf{A} that connects a successive pair of these snapshots as:

$$\mathbf{q}^{i+1} = \mathbf{A}\mathbf{q}^i, \quad i = \{0, \dots, M-1\}. \quad (7)$$

Introducing the matrices

$$\mathbf{Q}^0 = [\mathbf{q}^0 \ \mathbf{q}^1 \ \dots \ \mathbf{q}^{M-1}], \quad (8)$$

$$\mathbf{Q}^1 = [\mathbf{q}^1 \ \mathbf{q}^2 \ \dots \ \mathbf{q}^M], \quad (9)$$

and using equation (7) one has:

$$\mathbf{Q}^1 = \mathbf{A}\mathbf{Q}^0. \quad (10)$$

For reducing the degrees of freedom of the problem, as suggested by Schmid [14], the operator \mathbf{A} can be projected onto the r -dimensional POD basis \mathbf{U} of the snapshots matrix \mathbf{Q}^0 , calculated using a Singular Value Decomposition (SVD) or the snapshot method [33],

$$\mathbf{Q}^0 = \mathbf{U}\mathbf{S}\mathbf{V}^*. \quad (11)$$

Then, the matrix \mathbf{A} is approximated by

$$\mathbf{A} \approx \mathbf{U}\mathbf{F}\mathbf{U}^*, \quad (12)$$

where the matrix \mathbf{F} is obtained by minimizing the Frobenius norm of the difference between \mathbf{Q}^1 and $\mathbf{A}\mathbf{Q}^0$, as:

$$\min_{\mathbf{F}} \|\mathbf{Q}^1 - \mathbf{U}\mathbf{F}\mathbf{S}\mathbf{V}^*\|_F^2, \quad (13)$$

leading to the following optimal solution:

$$\mathbf{F} = \mathbf{U}^*\mathbf{Q}^1\mathbf{V}\mathbf{S}^{-1}. \quad (14)$$

Dynamic modes are then extracted by computing the eigendecomposition of the matrix \mathbf{F} :

$$\mathbf{F} = \underbrace{\begin{bmatrix} \mathbf{y}_1 & \dots & \mathbf{y}_r \end{bmatrix}}_{\mathbf{Y}} \underbrace{\begin{bmatrix} \mu_1 & & \\ & \ddots & \\ & & \mu_r \end{bmatrix}}_{\mathbf{D}_\mu} \underbrace{\begin{bmatrix} \mathbf{z}_1^* \\ \vdots \\ \mathbf{z}_r^* \end{bmatrix}}_{\mathbf{Z}^*}, \quad (15)$$

\mathbf{y}_i and \mathbf{z}_i^* being the right and left eigenvectors of \mathbf{F} , normalized as $\mathbf{y}_i^*\mathbf{y}_i = 1$ and $\mathbf{z}_i^*\mathbf{y}_j = \delta_{ij}$. Finally, the dynamics in the low-dimensional POD subspace, $\mathbf{x}^{i+1} = \mathbf{F}\mathbf{x}^i$ can be expressed as follows:

$$\mathbf{x}^n = \mathbf{Y}\mathbf{D}_\mu^n\mathbf{Z}^*\mathbf{x}^0 = \sum_i^r \mathbf{y}_i\mu_i^n\mathbf{z}_i^*\mathbf{x}^0 = \sum_i^r \mathbf{y}_i\mu_i^n\alpha_i, \quad (16)$$

where $\alpha_i = \mathbf{z}_i^*\mathbf{x}^0$ represents the component of the initial condition in the POD subspace, \mathbf{x}^0 , in the \mathbf{z}_i^* direction. Thus, the snapshots can be expanded as a linear combination of the DMD modes $\phi_i = \mathbf{U}\mathbf{y}_i$ as:

$$\mathbf{q}^n \approx \mathbf{U}\mathbf{x}^n = \sum_i^r \mathbf{U}\mathbf{y}_i\mu_i^n\alpha_i = \sum_i^r \phi_i\mu_i^n\alpha_i, \quad (17)$$

where α_i is the amplitude of the corresponding DMD mode. Equation (17) can be written in matrix form:

$$\underbrace{\begin{bmatrix} \mathbf{q}^0 & \mathbf{q}^1 & \dots & \mathbf{q}^{M-1} \end{bmatrix}}_{\mathbf{Q}^0} \approx \underbrace{\begin{bmatrix} \phi_1 & \phi_2 & \dots & \phi_r \end{bmatrix}}_{\Phi} \underbrace{\begin{bmatrix} \alpha_1 & & & \\ & \alpha_2 & & \\ & & \ddots & \\ & & & \alpha_r \end{bmatrix}}_{\mathbf{D}_\alpha} \underbrace{\begin{bmatrix} 1 & \mu_1 & \dots & \mu_1^{M-1} \\ 1 & \mu_2 & \dots & \mu_2^{M-1} \\ \vdots & \vdots & \ddots & \vdots \\ 1 & \mu_r & \dots & \mu_r^{M-1} \end{bmatrix}}_{\mathbf{V}_{and}}, \quad (18)$$

where \mathbf{V}_{and} is the Vandermonde matrix and $\Phi := \mathbf{U}\mathbf{Y}$ is the matrix composed of the DMD modes ϕ_i . The associated amplitudes $\alpha = [\alpha_1 \dots \alpha_r]^T$ are then computed by minimizing the

Frobenius norm of the difference between the left and the right size of equation (18), which can be performed in the low-dimensional POD subspace by using the eigendecomposition in equation (15), as:

$$\min_{\alpha} J(\alpha) = \|\mathbf{S}\mathbf{V}^* - \mathbf{Y}\mathbf{D}_{\alpha}\mathbf{V}_{and}\|_F^2. \quad (19)$$

Superposing the computed DMD modes, weighted by their amplitudes and oscillating at the obtained frequency and growth rate, allows one to optimally approximate the data sequence. However, when aiming at finding a low dimensional representation of the snapshots' sequence, the objective function $J(\alpha)$ in (19) should be augmented with an additional term that penalizes the number of non-zero elements in the amplitudes' vector α , as:

$$\min_{\alpha} J(\alpha) + \gamma \sum_{i=1}^r |\alpha_i|, \quad (20)$$

163 where γ is a parameter that influences the sparsity level, higher values of the parameter pro-
 164 moting sparser solutions. The resulting sparsity-promoting DMD problem in equation (20) is
 165 a convex optimization problem, solved using the Alternating Direction Method of Multipliers
 166 [24].

167 3. Simulation layout

168 3.1. Precursor simulation

169 In order to mimic a turbulent ABL impinging on the turbine, the precursor simulation is per-
 170 formed at $Re_{bulk} = U_{bulk}D/\nu = 10^8$, which is the same value used for the turbine wake flow
 171 simulation with uniform laminar inlet. The computational domain has dimensions $6 \times 5 \times 3$ di-
 172 ameter units in the streamwise, vertical and spanwise directions, respectively. No-slip boundary
 173 conditions are imposed at the bottom wall, whereas, at the top wall, vertical velocity and shear
 174 are set to zero. Periodicity is imposed in streamwise and spanwise directions. A staggered ar-
 175 ray of cubes with height $h_c = 0.1$ diameters is placed at the bottom wall of a turbulent channel
 176 [27] to trigger turbulence. Figure 1 provides a detailed description of the cubes arrangement,
 177 whereas figure 2(a) provides a cross section of the time-averaged streamwise velocity contours,
 178 showing the influence of the cubes at the wall and the presence of large-scale flow structures.
 179 Note that the bottom wall is placed at $y = -0.714$ diameters, in order to have the origin of the
 180 vertical direction corresponding to the hub height in the turbine wake simulation. The time-
 181 and space-averaged (in a cross section) streamwise velocity profile provided in the left panel of
 182 figure 2 (b) appears well fitted with a logarithmic law in the inner region, except for $y < -0.65$,
 183 where the roughness elements are present. Whereas, the profile in the outer region is well de-
 184 scribed by a power law having shear coefficient $\alpha = 0.27$. The turbulence intensity (I) profile
 185 is provided in the right panel of Figure 2 (b) and shows a turbulence intensity of approximately
 186 10% at the hub height. The corresponding time-varying turbulent velocity obtained by the pre-
 187 cursor simulation is imposed at the inlet of the turbine flow computational domain, as specified
 188 in the following.

189 3.2. Turbine flow LES

190 We consider the NREL-5MW wind turbine with a tip-speed ratio $\lambda = 7$ and Reynolds
 191 number $Re = 10^8$. The computational domain has dimensions $12.5 \times 5 \times 3$ diameters in
 192 x, y, z , respectively, as shown in figure 3. The turbine is centered in the transverse direction,

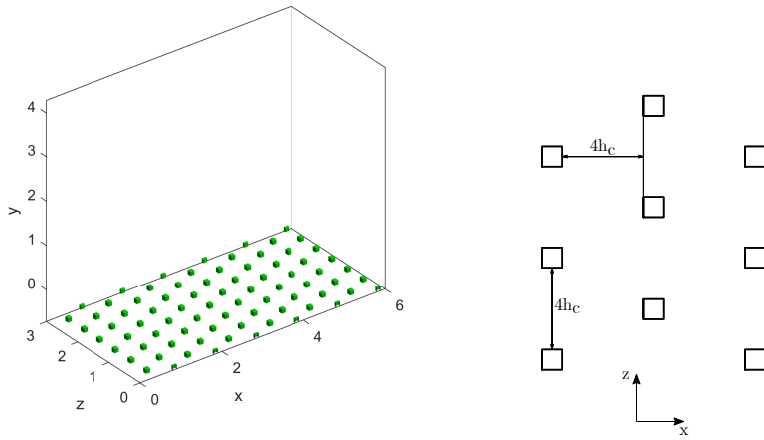


Figure 1: Layout of the precursor simulation reporting the arrangement of the cubes mounted at the wall.

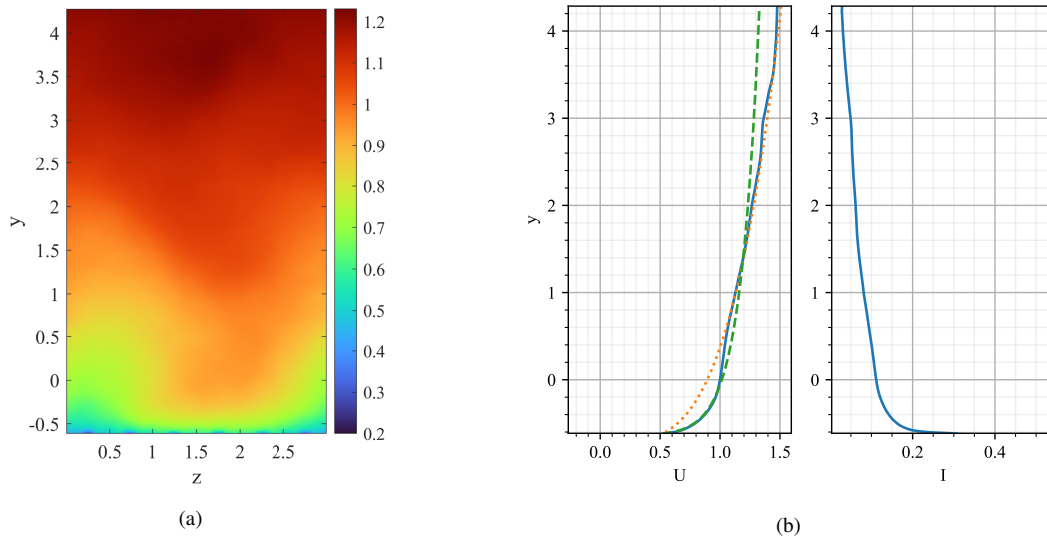


Figure 2: (a) Time-averaged streamwise velocity contours in a cross section of the precursor simulation computational domain. (b) Time- and space-averaged axial velocity and turbulent intensity profiles of the precursor (blue solid lines). The green dashed line is the log-law and the orange dotted line the power law of the wind profile. Note that in both figures, the region below the cubes' height is not shown.

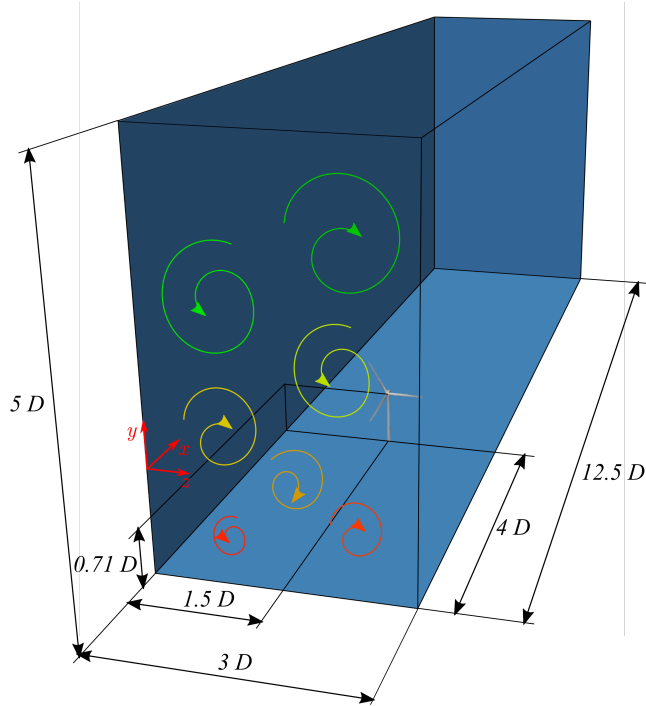


Figure 3: Computational domain and setting of the turbine wake LES. The coloured vortices represent the turbulent inflow.

193 and is located at 4 diameters from the inlet, where a uniform velocity U_∞ or the previously
 194 obtained turbulent profile is imposed. Note that in the latter case, due to turbulence decay, the
 195 turbulence intensity that impinges on the turbine is lower than 10% at the hub height. The
 196 computational domain is discretised by grid consisting of $2048 \times 512 \times 512$ grid-points in
 197 the x, y, z directions, respectively. The grid is uniform along the streamwise and transverse
 198 directions, and it is stretched in the vertical direction, with finer grid spacing in the turbine
 199 wake region.

200 4. DMD results

201 4.1. Turbine wake with uniform inflow

202 The DMD analysis of the wake of the NREL-5MW wind turbine with uniform incoming
 203 flow has been discussed in detail in Ref. [34]. We provide here the main results, which are
 204 relevant for the comparison with the case of a turbulent incoming flow. Snapshots of the veloc-
 205 ity field are extracted in a reduced three-dimensional subdomain of extent $[0 - 8.4] \times [-0.7 -$
 206 $0.63] \times [0.8 - 2.2]$ in the x, y and z direction, respectively, every Δt corresponding to a 10°
 207 rotation of rotor. The dataset is made by 3052 snapshots, whose ensemble average is subtracted
 208 from each snapshot before applying the DMD procedure. As a consequence, all the eigenval-
 209 ues lie on the unitary circle, as shown in the left panel of figure 4, providing the eigenvalues,
 210 μ , of the linear operator \mathbf{F} (see equation (15)). The frequency and growth rate of the DMD
 211 modes are shown in the right panel of figure 4. The modes selected by the sparsity-promoting
 212 algorithm for $\gamma = 40000$ are marked with a black circle. For this high value of γ , five pairs
 213 of DMD modes are selected, which are shown in figure 5. The second frame shows the mode
 214 having $\Re(\omega) = 42$, which is clearly related to the tip vortices and oscillates at an angular fre-
 215 quency equal to three times that of the turbine (due to the number of blades). The remaining

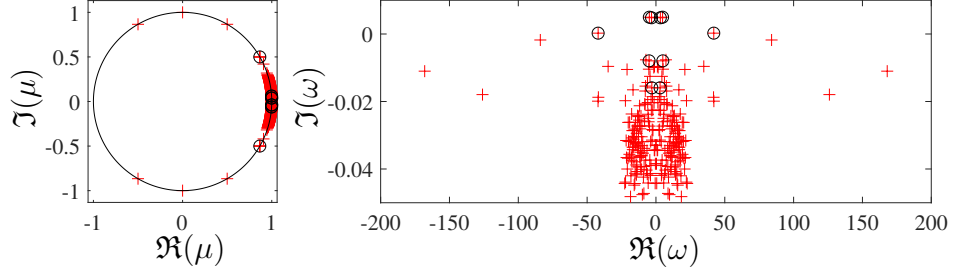


Figure 4: Eigenvalues resulting from the standard DMD algorithm (red crosses) and the sparsity promoting algorithm (black circles) for the case with laminar uniform inflow. The right panel shows the logarithmic mapping of the eigenvalues, $\omega = -\frac{\log(\mu)}{i\Delta t}$, where Δt is the time interval between two consecutive snapshots and i is the imaginary unit.

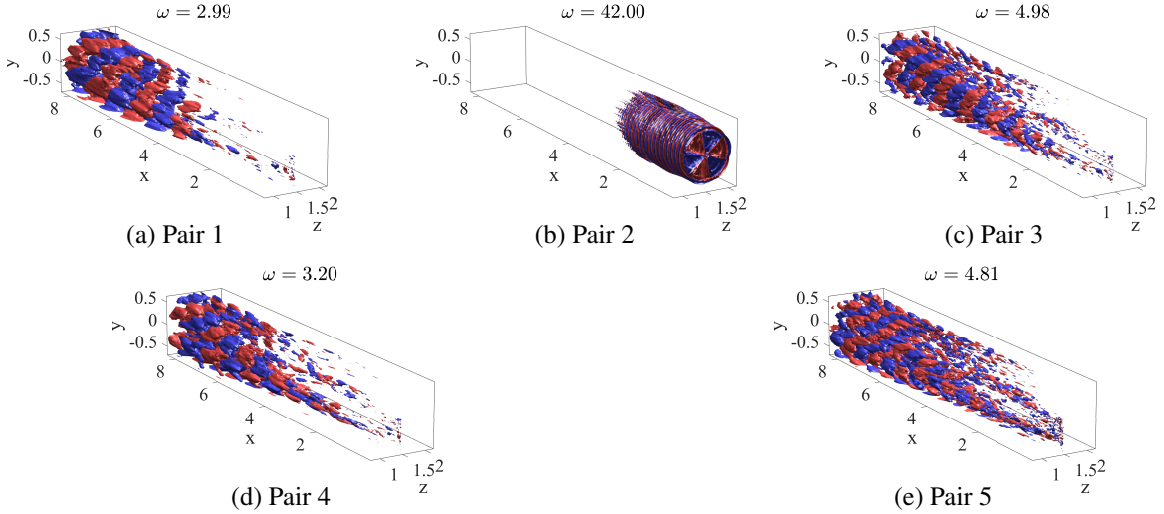
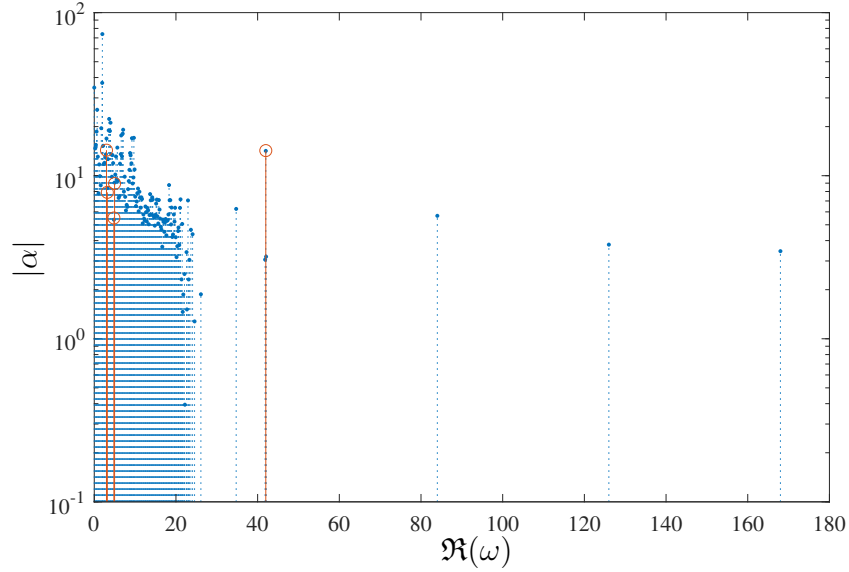


Figure 5: Streamwise velocity iso-surfaces (red for positive, blue for negative values) of the real part of the 5 dynamic modes' pairs selected by the sparsity-promoting algorithm for $\gamma = 40000$ and for the laminar uniform inflow, ordered according to their amplitude $|\alpha|$.

216 selected modes, having lower frequencies in the range $\Re(\omega) \in [2.99 - 4.97]$, are associated
 217 to spatial structures with moderate length scale, localized in the far wake region (see figure
 218 5(a, c-e)). For lower values of γ , as shown by the amplitude spectrum in figure 6, many other
 219 low-frequency modes are found. These modes present a spatial structure (not shown) similar
 220 to the moderate-scale modes previously shown, but associated to slightly higher/lower tempo-
 221 ral wavenumbers. High-frequency modes are present as well, mostly appearing as harmonics
 222 of the previously shown DMD mode associated to the tip vortices, provided in figure 5 (b).
 223 Some moderate-frequency modes ($\Re(\omega) \in [10 - 20]$) are present as well, mostly localized in
 224 the tower's and nacelle's wake and characterized by a fine spatial structures (not shown). A
 225 thorough discussion of these modes, which are used here as reference for the next considered
 226 cases, can be found in Ref. [34].

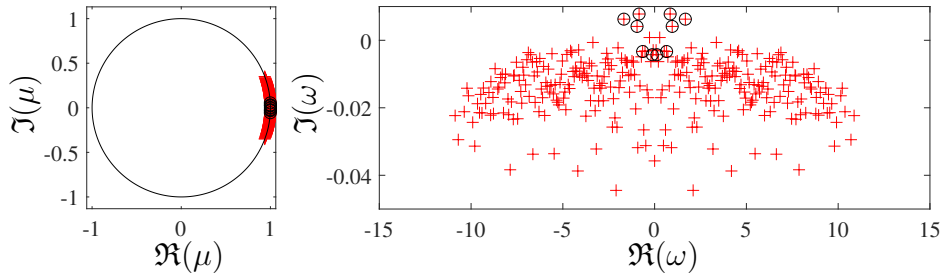
227 4.2. Precursor simulation

228 The DMD analysis has been applied to the precursor LES results by extracting the snapshots
 229 every $\Delta t = 0.033$ in a subdomain of size $[0 - 6.0] \times [-0.7 - 0.63] \times [0.8 - 2.2]$ in the x , y and z
 230 direction, respectively. The complete data-set is composed of 2990 snapshots. The convergence



1

Figure 6: Dependence of the absolute value of the DMD amplitudes α_i on the angular frequency $\Re(\omega)$, for the case with laminar inflow. The results are obtained using the standard (blue stems) and the sparsity-promoting algorithm with $\gamma = 40000$ (orange stems). Due to the symmetry of amplitudes' distribution, only positive frequencies are shown.

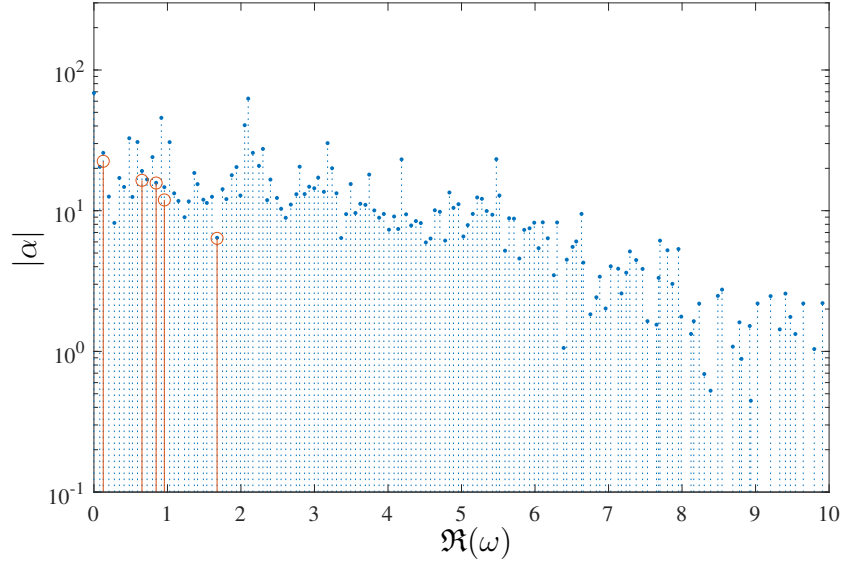


1

Figure 7: Eigenvalues resulting from the standard DMD algorithm (red crosses) and the sparsity promoting algorithm (black circles) for the precursor simulation. The right panel shows the logarithmic mapping of the eigenvalues, $\omega = -\frac{\log(\mu)}{i\Delta t}$, where Δt is the time interval between two consecutive snapshots and i is the imaginary unit.

231 study, reported in the Appendix, indicates a good stabilization of the frequency values already
 232 for a POD subspace of dimension $r \geq 251$, whereas the growth rates are well approximated for
 233 $r > 300$. For this reason, in the following, we will use a POD basis of dimension $r = 301$. In
 234 the left panel of Figure 7, the eigenvalues μ of the linear operator \mathbf{F} are provided, along with
 235 the unit circle. The modes selected for $\gamma = 65000$ are marked with a black circle. Looking
 236 at the right frame of figure 7, providing the temporal wavenumber $\Re(\omega)$ of the modes, one
 237 can note that the DMD modes are all characterized by rather low frequencies ($|\Re(\omega)| < 10$)
 238 compared to the previous case, which reaches wavenumbers of order 10^2 . The amplitude of
 239 these low-frequency modes is provided in figure 8, showing that the highest amplitudes are
 240 concentrated at the lowest frequencies. The red circles indicate the five modes selected by the
 241 sparsity-promoting algorithm for $\gamma = 65000$. The spatial structures of these five selected pairs
 242 are shown in figure 9.

243 The lowest-frequency mode with $\Re(\omega) = 0.13$, shown in figure 9 (a), is characterized by



1

Figure 8: Dependence of the absolute value of the DMD amplitudes α_i on the angular frequency $\Re(\omega)$, for the precursor simulation. The results are obtained using the standard (blue stems) and the sparsity-promoting algorithm (orange stems). Due to the symmetry of amplitudes' distribution, only positive frequencies are shown.

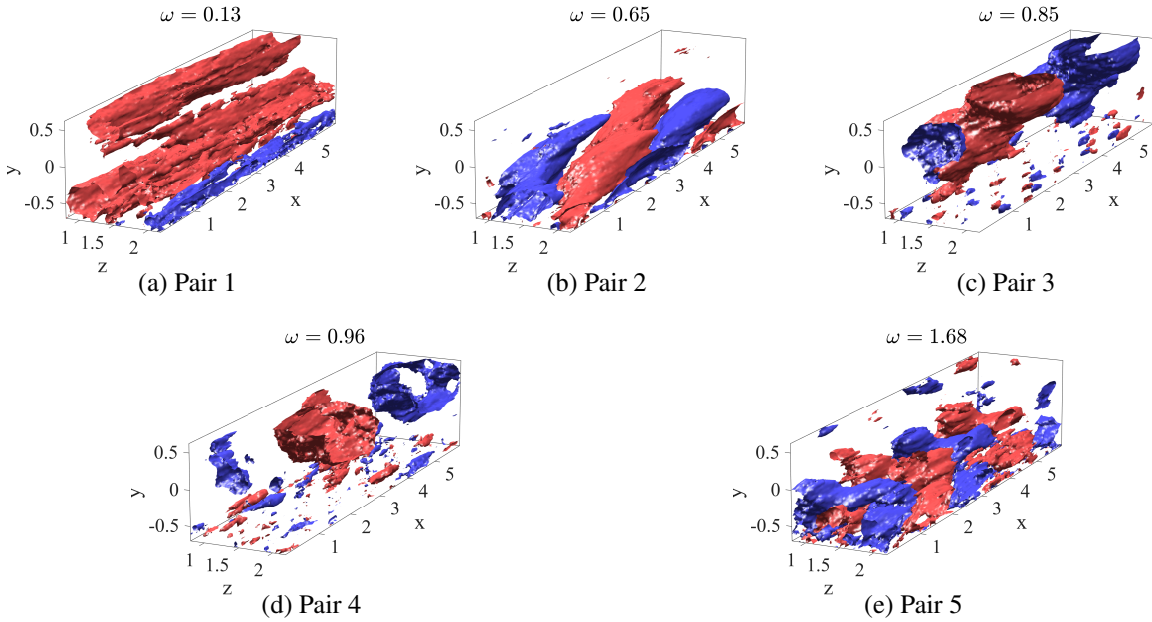


Figure 9: Streamwise velocity iso-surfaces (red for positive, blue for negative values) of the real part of the 5 dynamic modes' pairs selected by the sparsity-promoting algorithm, ordered according to their amplitude $|\alpha|$.

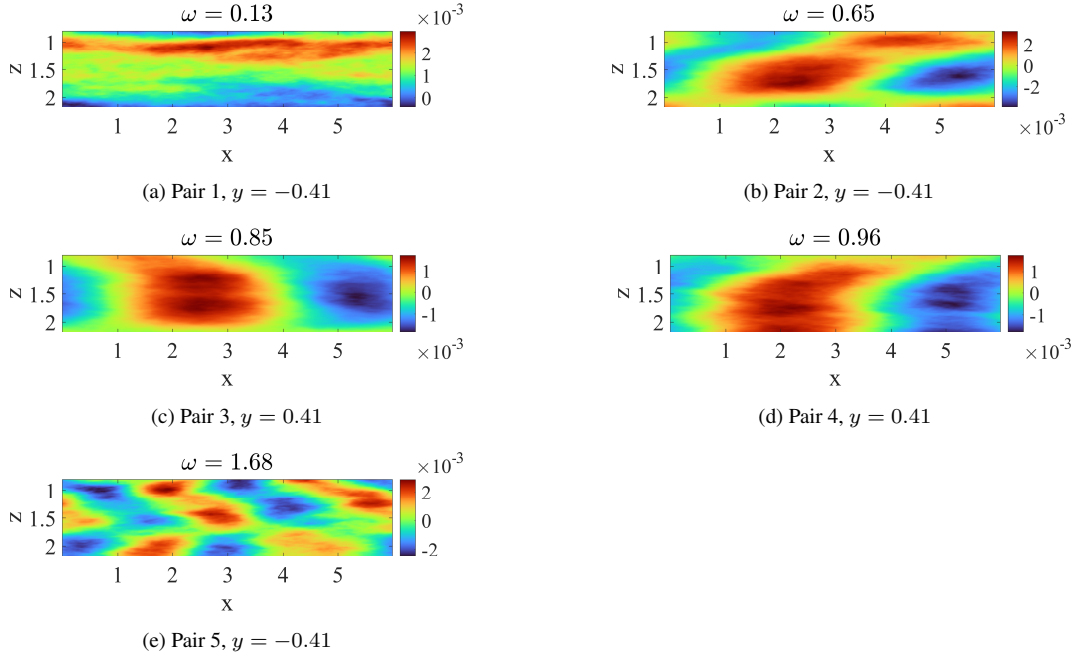


Figure 10: Streamwise velocity contours of the selected DMD modes for the precursor simulations in two different x - z planes.

244 high- and low-speed large-scale streaks of spanwise size ≈ 1 , which are known to constitute one
 245 of the two main elements of a self-sustained attached eddy characterizing the large-scale motion
 246 in shear flows [35]. Note that, since the DMD is carried out in a subdomain of the precursor
 247 computational domain, this DMD mode appears not to be composed of a complete pair of high-
 248 and low-speed large-scale streaks, but only a portion of the low-speed streak (blue surfaces) is
 249 visible in the considered subdomain. Nevertheless, the two-dimensional plots in the $x - z$ and
 250 $z - y$ planes, provided in figure 10 (a) and 11 (a), respectively, show the presence of portions of
 251 low-speed large-scale streaks on both sides of the high-speed one, so that the considered DMD
 252 mode appears to successfully capture the alternation of low- and high-speed large-scale streaks
 253 usually observed in turbulent shear flows. The successive mode, provided in figure 9 (b), is
 254 composed of oblique waves localized in the lowest part of the domain. Whereas, the two modes
 255 with $\Re(\omega) = 0.85, 0.96$, provided in figures 9 (c) and (d), respectively, are characterized by
 256 streamwise-modulated flow structures with rather large wave length ($\lambda_x \approx 5$) localized in the
 257 upper part of the domain, consistent with an undulation (or secondary instability, see [36]) of
 258 the low-frequency elongated streaks, associated with the presence of streamwise vortices. Two-
 259 dimensional plots of these three modes, provided in figures 10 (b-d) for two $x - z$ planes and
 260 figures 11 (b-d) for the $x = 2$ plane, show that these DMD modes have a very similar structure
 261 (despite being localized in different regions of the domain), and are probably thus linked to the
 262 same phenomenon, namely, the secondary instability of large-scale streaks. Finally, among the
 263 selected DMD modes, the highest-amplitude one is composed of slightly smaller structures,
 264 alternated in the streamwise direction and localized in the lowest part of the domain, as shown
 265 in figure 9 (e) and in figures 10 (e) and 11 (e). Notice that the length scales ($\lambda_z \approx 1 - 2$,
 266 $\lambda_x \approx 5 - 6$) of these dynamically relevant flow structures are consistent with those of the
 267 large-scale motion observed in turbulent channels and boundary layers [37, 38, 35, 39].

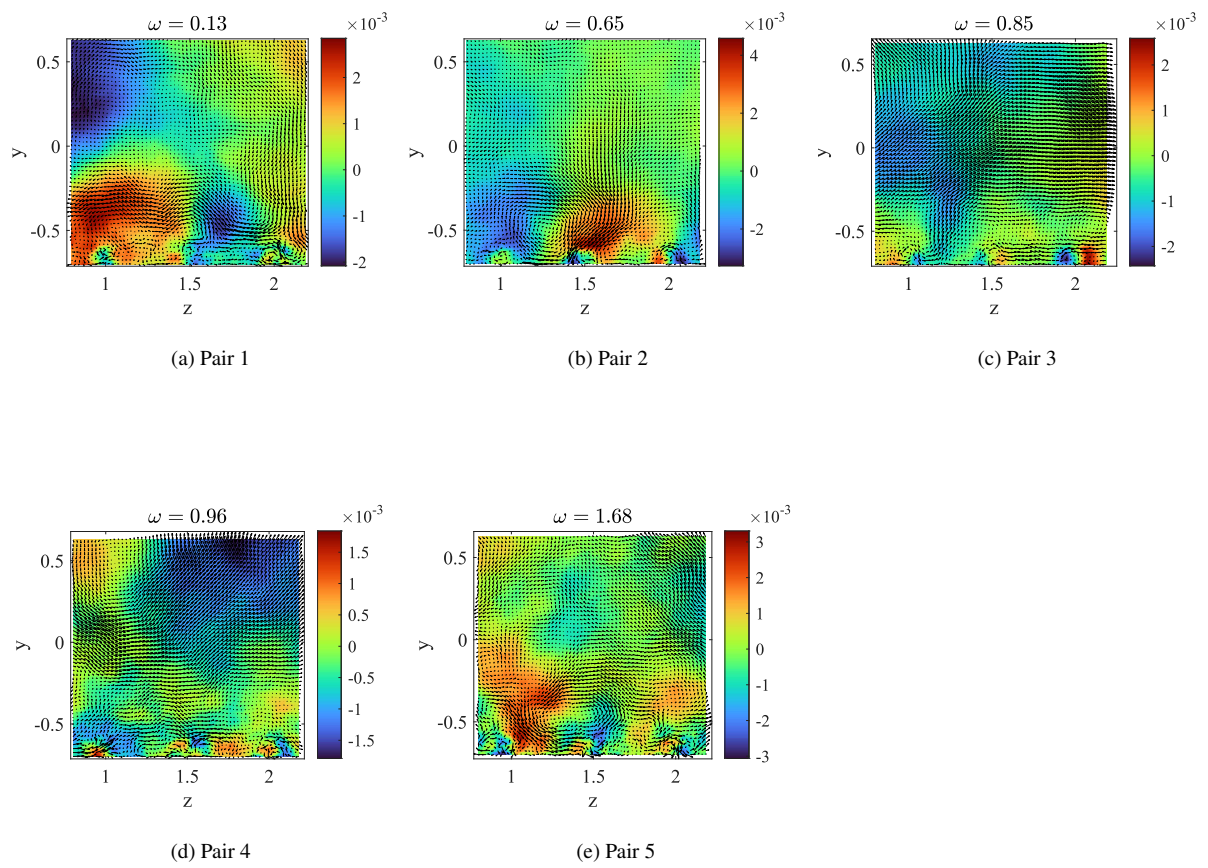


Figure 11: Streamwise velocity contours together with wall-normal and spanwise velocity vectors of the selected DMD modes for the precursor simulations in the $x = 2$ plane.

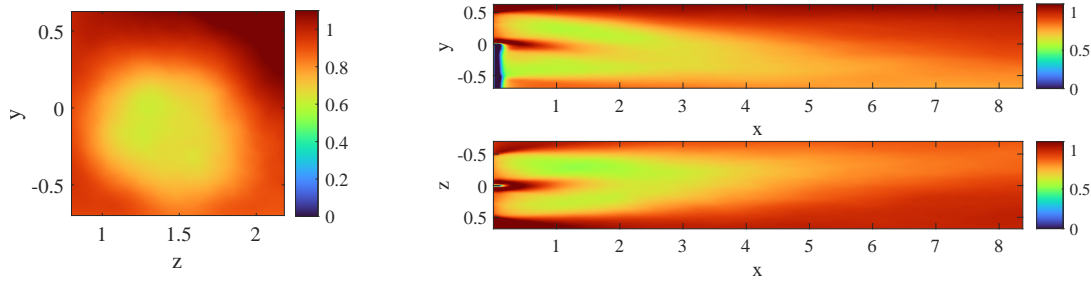


Figure 12: Ensemble average of the LES snapshots of the turbine’s wake simulation with inflow turbulence: streamwise velocity in the plane $x = 3$ (left), $y = 0$ (top right), and $z = 0$ (bottom right).

268 4.3. Turbine wake with turbulent inflow

269 In this section we analyze the DMD of the turbine wake in the presence of the turbulent
 270 incoming flow obtained by the precursor simulation. We take snapshots of the velocity field in a
 271 reduced three-dimensional subdomain enclosing the wake, with a sampling time corresponding
 272 to a 10° rotation of rotor. As in the previously discussed laminar-inflow case, the extent of the
 273 subdomain is $[0 - 8.4] \times [-0.7 - 0.63] \times [0.8 - 2.2]$ in the x , y and z direction, respectively.
 274 The entire data-set comprises 3052 snapshots, whose ensemble average (which is subtracted
 275 from each snapshot) is shown in Figure 12. One can observe that, due to the turbine rotation,
 276 the wake is asymmetric, deviating towards the left in the transverse direction, and towards the
 277 bottom in the vertical direction. The presence of a small wake right behind the tower can be
 278 highlighted as well. By means of a convergence study, reported in the Appendix, we have
 279 found a good convergence of the frequency values for a POD subspace of dimension $r > 600$,
 280 thus in the following we use $r = 601$. In the left panel of Figure 13 the eigenvalues μ of the
 281 linear operator \mathbf{F} are shown, along with the unit circle. Note that the growth rate of the modes
 282 is not exactly zero (as it should be when the mean flow is subtracted from the snapshots, see
 283 [40]) since the DMD is carried out on a projection of the flow fields on a POD subspace. The
 284 pairs selected by the sparsity-promoting algorithm for $\gamma = 65000$, marked with a black circle
 285 in the figure, are seven. Their amplitudes are provided in figure 14. From this figure one can
 286 observe that, despite some high-frequency modes (i.e., $\Re(\omega) = 28.5 - 42$) can be seen in the
 287 standard-DMD amplitude spectrum, these are not selected by the sparsity-promoting algorithm.
 288 This indicates that, in the presence of atmospheric turbulence, the high-frequency modes, such
 289 as tip vortices, become less relevant for the flow dynamics. The selected SP-DMD modes,
 290 ordered by their amplitude, are shown in figure 15. One can notice that all the selected
 291 modes, having low frequencies in the range $\Re(\omega) \in [0.37 - 4.23]$, are associated to large-
 292 scale spatial structures filling the whole subdomain. Compared with the DMD modes of the
 293 laminar-inflow case in figure 5(a, c-e), in the present case the structures have larger wavelengths
 294 and are not localized in the far wake but pervade the whole domain. While in the laminar-
 295 inflow case, the modes displayed a clear geometrical arrangement with respect to the turbine
 296 (namely, the tip vortices are localized in the near wake, and the low-frequency ones in the
 297 remainder of the domain), in the turbulent-inflow case, no spatial separation among the modes is
 298 observed. However, evidence of the presence of the turbine can be seen in some of the selected
 299 modes, as shown in figure 16 (c-d-e), since the oscillation clearly appear to be originated at $z =$
 300 $1, 1.5, 2$, where tip and root vortices are present. On the other hand, many of these modes bear
 301 a strong resemblance with those selected by the sparsity-promoting algorithm in the precursor
 302 simulation (see figure 9 (b-e)). Concerning their main wavelengths, the DMD modes with

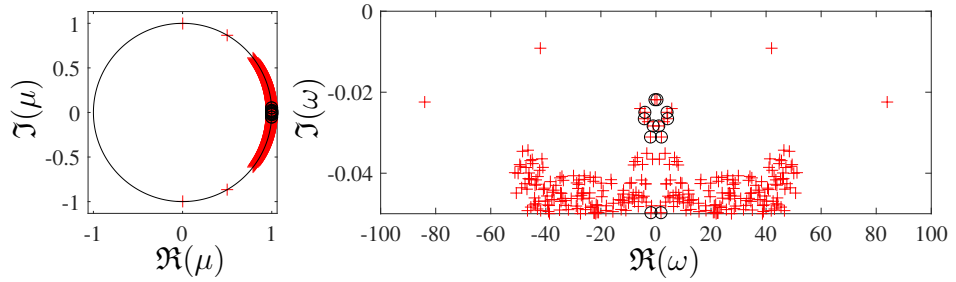


Figure 13: Eigenvalues resulting from the standard DMD algorithm (red crosses) and the sparsity promoting algorithm (black circles) for the case with turbulent inflow. The right panel shows the logarithmic mapping of the eigenvalues, $\omega = -\frac{\log(\mu)}{i\Delta t}$, where Δt is the time interval between two consecutive snapshots and i is the imaginary unit.

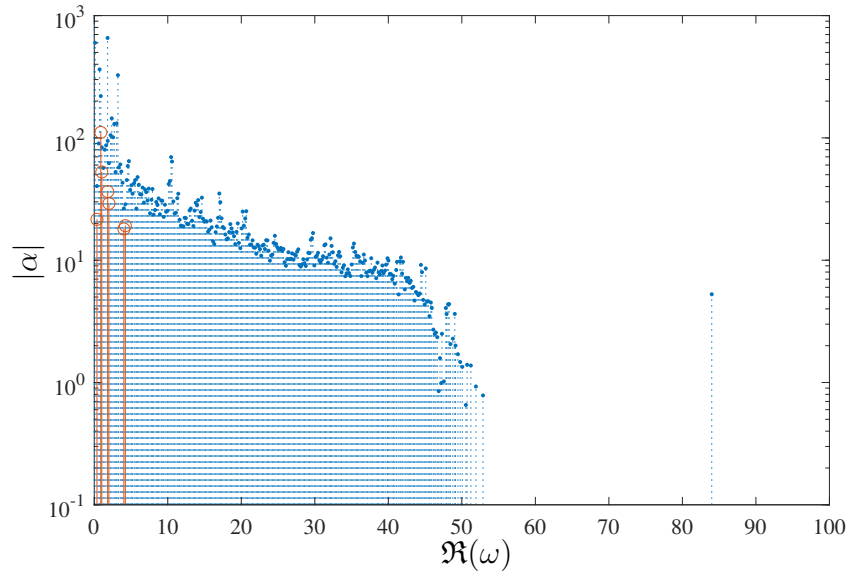


Figure 14: Dependence of the absolute value of the DMD amplitudes α_i on the angular frequency $\Re(\omega)$, for the case with turbulent inflow. The results are obtained using the standard (blue stems) and the sparsity-promoting algorithm (orange stems). Due to the symmetry of amplitudes' distribution, only positive frequencies are shown.

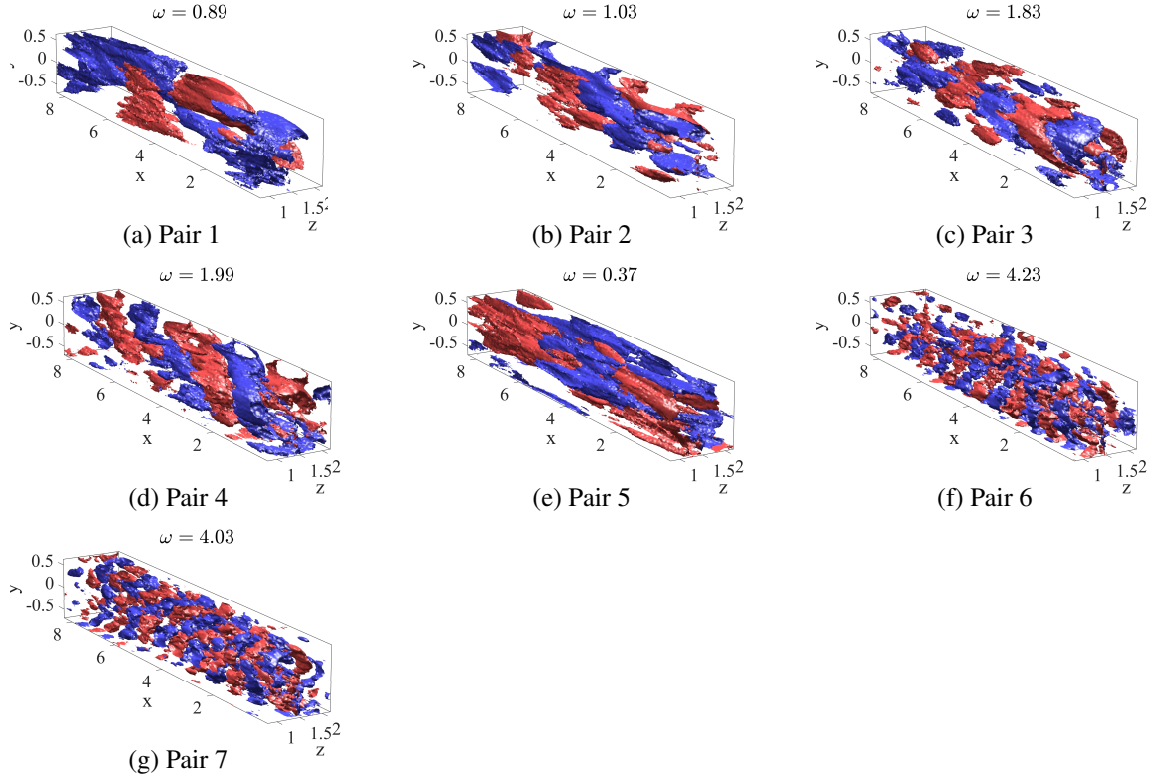


Figure 15: Streamwise velocity iso-surfaces (red for positive, blue for negative values) of the real part of the 8 dynamic modes' pairs selected by the sparsity-promoting algorithm, ordered according to their amplitude $|\alpha|$.

303 $\Re(\omega) = [0.37 - 0.89 - 1.03]$ provided in figure 15 (a-b-e), show streamwise oscillations
 304 with $\lambda_x \approx 7$ and spanwise size ≈ 1 , similarly to those selected in the precursor simulation
 305 (compare also figure 16 (a-b-e) with figure 10 (b-c-d)). Moreover, all the modes characterized
 306 by very low frequency ($\Re(\omega) \leq 1$) have a Strouhal number $St \leq 0.2$, which lies well within
 307 the frequency range typical of the wake meandering [41, 42, 43]. This suggests that wake
 308 meandering is due rather to an exogenous mechanism than to an endogenous one, as proposed
 309 in recent works [42, 43]. Finer structures are observed for the modes having larger frequencies
 310 in the range $\Re(\omega) = [1.83 - 4.03]$, resembling those found in the laminar-inflow case at similar
 311 frequencies (see figure 6 (d-e)), although not presenting a spatial localization in the far wake.
 312 The temporal wavenumbers and the streamwise wavelengths of the first five selected SP-DMD
 313 modes, compared to those of the laminar-inflow and the precursor simulations, are summarized
 314 in table 1. One can clearly notice that, somehow counter-intuitively, the presence of turbulence
 315 at the inflow induces an increase of the main wavelengths from values equal or lower than 2.1,
 316 to values larger than ≈ 3.4 .

317 In order to validate these findings, we have carried out the sparsity-promoting DMD analy-
 318 sis for lower values of γ , selecting an increasing number of modes for both the laminar and the
 319 turbulent inflow cases. The comparison of the resulting DMD spectra, provided in figure 17
 320 (a) for ≈ 50 modes, clearly shows that, even when many modes are selected, in the turbulent-
 321 inflow case the high-frequency modes are not selected by the sparsity-promoting DMD al-
 322 gorithm, suggesting that they have lost their dynamical relevance with respect to the laminar
 323 inflow case. Moreover, the comparison of the mode amplitudes in figure 17 (b) clearly shows
 324 that in the turbulent case the low-frequency modes are associated with much higher amplitudes

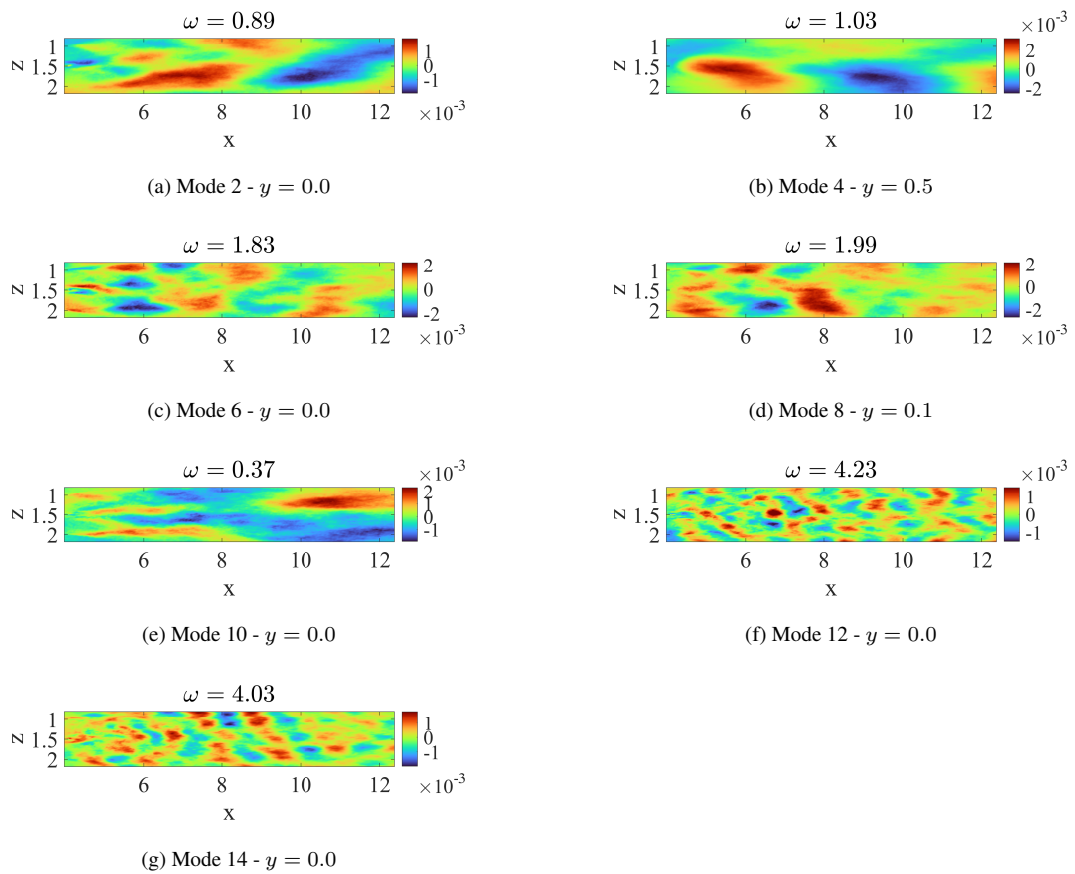


Figure 16: Streamwise velocity contours of the selected DMD modes for the turbulent inflow simulation in different x - z planes.

Table 1: Temporal frequencies and main wavelengths of the selected complex conjugate dynamic modes' pairs for the laminar-inflow, the precursor, and the turbulent-inflow simulation.

	Laminar inflow		Precursor		Turbulent Inflow	
	$\Re(\omega)$	λ_x	$\Re(\omega)$	λ_x	$\Re(\omega)$	λ_x
Pair 1	2.99	2.10	0.13	0	0.89	7.45
Pair 2	42	0.17	0.65	5.32	1.03	7.45
Pair 3	4.98	1.41	0.85	5.32	1.83	3.39
Pair 4	3.2	1.68	0.96	5.32	1.99	3.59
Pair 5	4.81	1.41	1.68	2.62	0.37	7.45

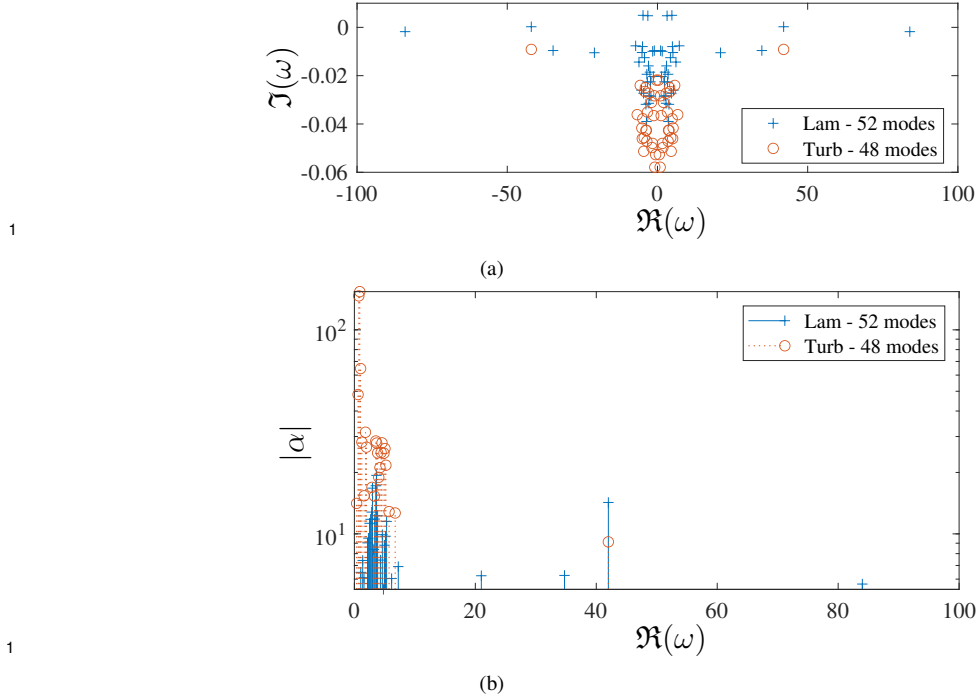


Figure 17: Comparison between the DMD eigenvalues spectra (a) and the mode amplitudes (b) computed for the cases with laminar and turbulent inflow with a particular γ able to select approximately 50 modes in both cases.

325 than in the laminar one. Similar results have been found for different values of γ . These results
326 indicate that, in the presence of atmospheric-like turbulence, high-frequency structures, such
327 as tip vortices, loose their dynamical relevance, being superseded by low-frequency modes
328 which have structures and frequencies lying in the range of the wake meandering. Therefore,
329 by the present analysis, we have clearly identified dynamically relevant coherent structures in
330 the turbine wake due to endogenous and exogenous effects. Moreover, the results indicate that
331 large-scale coherent structures with frequencies lying in the range of the wake meandering have
332 an exogenous origin.

333 5. Conclusions

334 The wake produced by a wind turbine is typically characterized by flow structures origi-
335 nated by endogenous mechanisms, such as the tip- and root-vortex helices or the von Kármán
336 street developing behind the tower. However, when the wind turbine operates in the atmo-
337 spheric boundary layer, its wake could be significantly affected by flow structures embedded

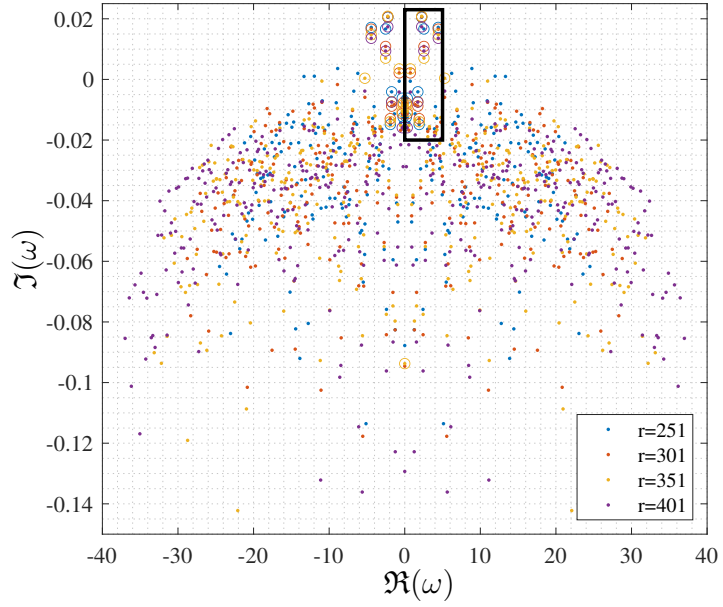
338 in the latter. These flow structures can be detected in the wind turbine wake, even though they
 339 are not directly generated by the turbine and are therefore due to exogenous phenomena. The
 340 present work investigates the dynamical relevance of coherent structures arising from endoge-
 341 nous and exogenous mechanisms in an NREL-5MW wind turbine’s wake under the effect of a
 342 turbulent inflow. For the first time, we apply the Sparsity-Promoting Dynamic Mode Decom-
 343 position (SP-DMD) to a wind turbine wake; SP-DMD is based on snapshots extracted from
 344 large-eddy simulations of the turbine wake, and used for detecting dynamically-relevant flow
 345 structures in the presence and in the absence of atmospheric turbulence.

346 Analysing the selected SP-DMD modes, we demonstrate that inflow turbulence strongly
 347 affects the dynamics of the wake, leading to the dynamical prevalence of structures due to
 348 exogenous mechanisms and to the detriment of those linked to endogenous ones. When a
 349 uniform laminar flow is imposed at the inlet, the most dynamically relevant modes coincide
 350 with the high-frequency tip vortices with temporal wavenumber equal to 42 and wavelength
 351 ≈ 0.1 , localized in the near wake. Moreover, moderate-scale coherent structures are found,
 352 localized in the far wake, having temporal wavenumber $\Re(\omega) \in [3-5]$ and wavelength of order
 353 1. In the presence of inflow turbulence, high-frequency structures, such as the tip vortices, are
 354 superseded by large-scale structures having low frequencies in the range $\Re(\omega) \in [0.3-1.6]$ and
 355 wavelength ≈ 7 , and by a few moderate-scale modes having higher frequency, $\Re(\omega) \in [3-5]$,
 356 and wavelength ≈ 1 , which now fill the whole domain. The DMD analysis of the precursor
 357 simulation shows that the low-frequency modes, detected in the turbine wake in the presence of
 358 inflow turbulence, roughly correspond to the most dynamically relevant modes for the turbulent
 359 flow upstream of the turbine.

360 These results indicate that structures originating from endogenous mechanisms, such as tip
 361 and root vortices, lose their dynamical relevance when turbulence impinges on the turbine,
 362 being superseded by large-scale coherent structures with frequencies lying in the range of the
 363 wake meandering. SP-DMD has been applied to a wind turbine wake, allowing us to separate
 364 endogenous and exogenous effects and to verify that wave meandering is due to exogenous
 365 flow fluctuations already present in the atmospheric boundary layer. Thus, accurate Reduced-
 366 Order Models (ROM) of utility-scale wind turbines should take into due account the presence
 367 of coherent structures embedded in the flow upstream of the turbine. These advanced ROMs
 368 will be crucial for: (i) designing modern wind farm with enhanced energy production capacity;
 369 (ii) developing real-time active control strategy for “smart” wind farm. Therefore, future work
 370 will aim at developing DMD-based reduced-order models in the presence of turbulent inflow.

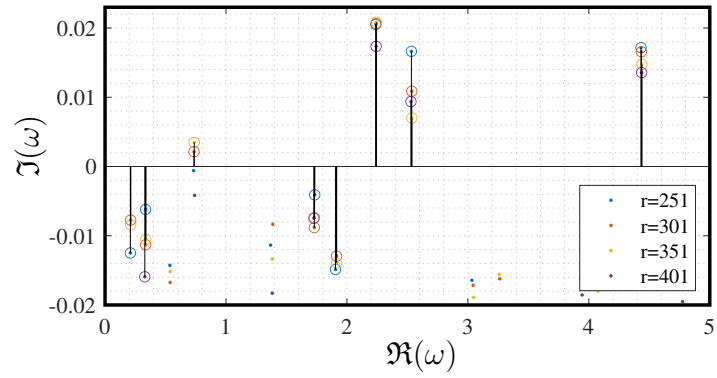
371 **Appendix A. Convergence with respect to the POD subspace dimension**

372 The influence of the dimension of the POD subspace on the DMD modes for the laminar
 373 inflow case has been investigated in [34], showing a good convergence of the DMD spectrum
 374 for a POD subspace dimension $r > 300$. Here we show the convergence of the DMD spectrum
 375 with respect to r for the precursor simulation (figure 18) and for the turbulent inflow case (figure
 376 19). Figure 18 shows the entire spectrum along with a close-up for the precursor simulation
 377 with four values of r ranging from 251 to 401. The close-up in the bottom frame shows that
 378 a good convergence of the frequencies is found already for a POD subspace of dimension
 379 $r > 250$, whereas the growth rates are well approximated for $r > 300$. The DMD spectrum
 380 for the turbulent inflow case, for values of r ranging from 501 to 701, is shown in figure 19.
 381 The results indicate that a good convergence of the frequencies as well as of the growth rate is



1

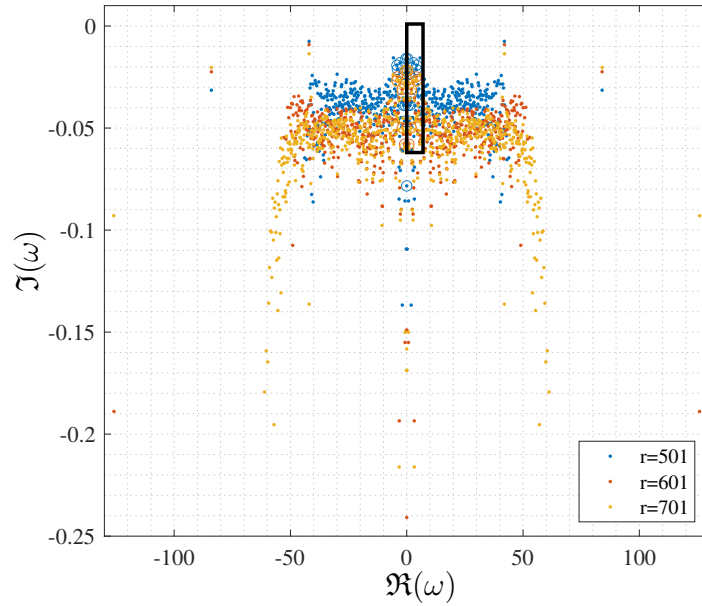
(a)



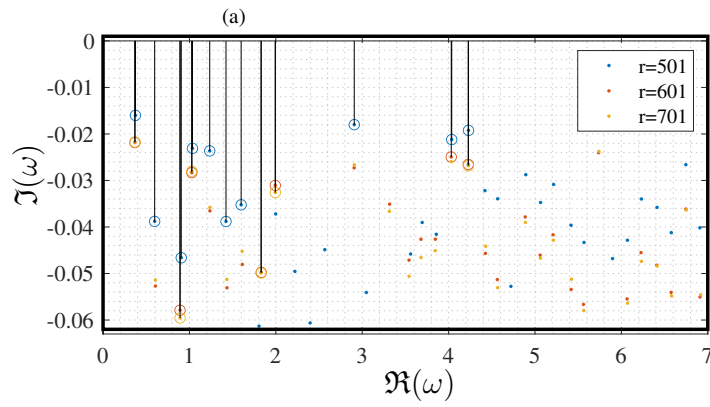
1

(b)

Figure 18: Convergence of the DMD spectrum with respect to the dimension r of the POD basis for the ABL precursor.



1



1

(b)

Figure 19: Convergence of the DMD spectrum with respect to the dimension r of the POD basis for the case with turbulent inlet velocity.

382 obtained for a POD subspace of dimension $r \geq 601$, which has been chosen for the analysis
383 presented in this work.

384 **References**

- 385 [1] IREA, Future of wind: Deployment, investment, technology, grid integration and socio-
386 economic aspects (a global energy transformation paper), Technical Report, International
387 Renewable Energy Agency, 2019.
- 388 [2] IEA, Renewable 2020, analysis and forecast to 2025. Fuel report., Technical Report, In-
389 ternational Energy Agency, 2020.
- 390 [3] R. J. Stevens, C. Meneveau, Flow structure and turbulence in wind farms, *Annual review*
391 *of fluid mechanics* 49 (2017) 311–339.
- 392 [4] F. Porté-Agel, M. Bastankhah, S. Shamsoddin, Wind-turbine and wind-farm flows: A
393 review, *Boundary-Layer Meteorology* (2019) 1–59.
- 394 [5] W. Munters, J. Meyers, An optimal control framework for dynamic induction control
395 of wind farms and their interaction with the atmospheric boundary layer, *Phylosophical*
396 *Transactions A* 375 (2017) 20160100.
- 397 [6] C. Cossu, Wake redirection at higher axial induction, *Wind Energy Science* 6 (2021)
398 377–388.
- 399 [7] U. Ciri, M. A. Rotea, S. Leonardi, Effect of the turbine scale on yaw control, *Wind*
400 *Energy* 21 (2018) 1395–1405.
- 401 [8] E. Kleusberg, S. Bernard, D. S. Henningson, Tip-vortex breakdown of wind turbines
402 subject to shear, *Wind Energy* 22 (2019) 1789–1799.
- 403 [9] N. Troldborg, J. N. Sørensen, R. F. Mikkelsen, Actuator line simulation of wake of wind
404 turbine operating in turbulent inflow, *Journal of Physics: Conference Series* 75 (2007)
405 012063.
- 406 [10] L. P. Chamorro, F. Porté-Agel, Effects of thermal stability and incoming boundary-layer
407 flow characteristics on wind-turbine wakes: A wind-tunnel study., *Boundary-layer mete-*
408 *orology* 136 (2010) 515–533.
- 409 [11] D. Medici, P. Alfredsson, Measurements on a wind turbine wake: 3D effects and bluff
410 body vortex shedding, *Wind Energy: An International Journal for Progress and Applica-*
411 *tions in Wind Power Conversion Technology* 9 (2006) 219–236.
- 412 [12] Y.-T. Wu, F. Porté-Agel, Atmospheric turbulence effects on wind-turbine wakes: An LES
413 study, *energies* 5 (2012) 5340–5362.
- 414 [13] J. Jonkman, S. Butterfield, W. Musial, G. Scott, Definition of a 5-MW refrence wind
415 turbine for offshore system development, Technical Report 38060, NREL-TP-500-38060,
416 2009.
- 417 [14] P. J. Schmid, Dynamic mode decomposition of numerical and experimental data, *Journal*
418 *of Fluid Mechanics* 656 (2010) 5–28.

- 419 [15] C. W. Rowley, I. Mezić, S. Bagheri, P. Schlatter, D. S. Henningson, Spectral analysis of
420 nonlinear flows, *Journal of Fluid Mechanics* 641 (2009) 115–127.
- 421 [16] G. V. Iungo, C. Santoni-Ortiz, M. Abkar, F. Porté-Agel, M. A. Rotea, S. Leonardi, Data-
422 driven reduced order model for prediction of wind turbine wakes, *Journal of Physics:*
423 *Conference Series* 625 (2015) 012009.
- 424 [17] M. Debnath, C. Santoni, S. Leonardi, G. V. Iungo, Towards reduced order modelling for
425 predicting the dynamics of coherent vorticity structures within wind turbine wakes, *Philo-*
426 *sophical Transactions of the Royal Society A: Mathematical, Physical and Engineering*
427 *Sciences* 375 (2017).
- 428 [18] S. Le Clainche, L. S. Lorente, J. M. Vega, Wind predictions upstream wind turbines from
429 a lidar database, *Energies* 11 (2018) 543.
- 430 [19] J. N. Kutz, S. L. Brunton, B. W. Brunton, J. L. Proctor, Dynamic mode decomposition:
431 data-driven modeling of complex systems, SIAM, 2016.
- 432 [20] S. Sarmast, R. Dadfar, R. F. Mikkelsen, P. Schlatter, S. Ivanell, J. N. Sørensen, D. S.
433 Henningson, Mutual inductance instability of the tip vortices behind a wind turbine,
434 *Journal of Fluid Mechanics* 755 (2014) 705–731.
- 435 [21] P. Premaratne, H. Hu, Analysis of turbine wake characteristics using dynamic mode
436 decomposition, in: *35th AIAA Applied Aerodynamics Conference*, AIAA, 2017, pp.
437 2017–4214.
- 438 [22] V. G. Kleine, E. Kleusberg, A. Hanifi, D. S. Henningson, Tip-vortex instabilities of two
439 in-line wind turbines, in: *Journal of Physics: Conference Series*, volume 1256, IOP
440 Publishing, 2019, p. 012015.
- 441 [23] C. Sun, T. Tian, X. Zhu, O. Hua, Z. Du, Investigation of the near wake of a horizontal-axis
442 wind turbine model by dynamic mode decomposition, *Energy* 227 (2021) 120418.
- 443 [24] M. R. Jovanović, P. J. Schmid, J. W. Nichols, Sparsity-promoting dynamic mode decom-
444 position, *Physics of Fluids* 26 (2014) 024103.
- 445 [25] C. Santoni, K. Carrasquillo, I. Arenas-Navarro, S. Leonardi, Effect of tower and nacelle
446 on the flow past a wind turbine, *Wind Energy* 20 (2017) 1927–1939.
- 447 [26] G. De Cillis, S. Cherubini, O. Semeraro, S. Leonardi, P. De Palma, POD-based analysis
448 of a wind turbine wake under the influence of tower and nacelle, *Wind Energy* 24 (2021)
449 609–633.
- 450 [27] W.-C. Cheng, F. Porté-Agel, Adjustment of turbulent boundary-layer flow to idealized
451 urban surfaces: A large-eddy simulation study, *Boundary-Layer Meteorology* 155 (2015)
452 249–270.
- 453 [28] P. Orlandi, *Fluid flow phenomena: a numerical toolkit*, volume 55, Springer Science &
454 Business Media, 2012.

- 455 [29] J. N. Sørensen, W. Z. Shen, Computation of wind turbine wakes using combined navier-
456 stokes/actuator-line methodology, in: 1999 European Wind Energy Conference and Ex-
457 hibition, 1999, pp. 156–159.
- 458 [30] M. D. de Tullio, P. De Palma, G. Iaccarino, G. Pascazio, M. Napolitano, An immersed
459 boundary method for compressible flows using local grid refinement, *Journal of Compu-
460 tational Physics* 225 (2007) 2098–2117.
- 461 [31] P. Orlandi, S. Leonardi, DNS of turbulent channel flows with two-and three-dimensional
462 roughness, *Journal of Turbulence* (2006) N73.
- 463 [32] C. Santoni, E. J. García-Cartagena, U. Ciri, L. Zhan, G. V. Iungo, S. Leonardi, One-way
464 mesoscale-microscale coupling for simulating a wind farm in north texas: Assessment
465 against SCADA and LiDAR data, *Wind Energy* 23 (2021) 691–710.
- 466 [33] L. Sirovich, Turbulence and the dynamics of coherent structures. Parts i-iii., *Quarterly of
467 applied mathematics* 45 (1987) 561–590.
- 468 [34] G. De Cillis, S. Cherubini, O. Semeraro, S. Leonardi, P. De Palma, DMD of the wake of
469 a NREL-5MW wind turbine, SDEWES Conference submitted to (2021).
- 470 [35] Y. Hwang, Statistical structure of self-sustaining attached eddies in turbulent channel
471 flow, *Journal of Fluid Mechanics* 767 (2015) 254–289.
- 472 [36] M. de Giovanetti, H. J. Sung, Y. Hwang, Streak instability in turbulent channel flow:
473 the seeding mechanism of large-scale motions, *Journal of Fluid Mechanics* 832 (2017)
474 483–513.
- 475 [37] L. S. G. Kovasznay, V. Kibens, R. F. Blackwelder, Large-scale motion in the intermittent
476 region of a turbulent boundary layer, *Journal of Fluid Mechanics* 41 (1970) 283–325.
- 477 [38] J. Lee, J. Lee, J. Choi, H. Sung, Spatial organization of large- and very-large-scale mo-
478 tions in a turbulent channel flow, *Journal of Fluid Mechanics* 749 (2014) 818–840.
- 479 [39] M. Farano, S. Cherubini, P. De Palma, J.-C. Robinet, Nonlinear optimal large-scale struc-
480 tures in turbulent channel flow, *European Journal of Mechanics - B/Fluids* 72 (2018)
481 74–86.
- 482 [40] K. K. Chen, J. H. Tu, C. W. Rowley, Variants of dynamic mode decomposition: Bound-
483 ary condition, Koopman, and Fourier analyses., *Journal of Nonlinear Science* 22 (2012)
484 887–915.
- 485 [41] D. Medici, Experimental studies of wind turbine wakes: power optimisation and mean-
486 dering, Ph.D. thesis, KTH, 2005.
- 487 [42] X. Mao, J. Sørensen, Far-wake meandering induced by atmospheric eddies in flow past a
488 wind turbine, *Journal of Fluid Mechanics* 846 (2018) 190–209.
- 489 [43] V. Gupta, M. Wan, Low-order modelling of wake meandering behind turbines, *Journal
490 of Fluid Mechanics* 877 (2019) 534–560.